Results in Physics 18 (2020) 103296

Contents lists available at ScienceDirect

Results in Physics

journal homepage: www.elsevier.com/locate/rinp

Cross coupled interlinked split ring resonator based epsilon negative metamaterial with high effective medium ratio for multiband satellite and radar communications

Md. Moniruzzaman[a,*], Mohammad Tariqul Islam[a,*], Md. Tarikul Islam[a], Muhammad E.H. Chowdhury[b,*], Hatem Rmili[c], Md. Samsuzzaman[d]

[a] Dept. of Electrical, Electronic and Systems Engineering, Faculty of Engineering and Built Environment, Universiti Kebangsaan Malaysia, Malaysia
[b] Department of Electrical Engineering, Qatar University, Doha 2713, Qatar
[c] King Abdulaziz University, Faculty of Engineering, Electrical and Computer Engineering Department, P.O. Box 80204, Jeddah 21589, Saudi Arabia
[d] Dept. of Computer and Communication Engineering, Faculty of Computer Science and Engineering, Patuakhali Science and Technology University, Bangladesh

ARTICLE INFO

Keywords:
Metamaterial
Split ring resonator
Epsilon negative
Effective medium ratio
Satellite and Radar communications

ABSTRACT

In this paper, a cross coupled interlinked split ring resonator based (CCI-SRR) based metamaterial has been presented. Epsilon negative (ENG) with a highly effective medium ratio (EMR) is attained in this metamaterial. The metamaterial unit cell consists of one square shaped split ring resonator and two rectangular rings. The rectangular rings reside within the outer square split ring. Two internal rings are coupled together by using a cross-shaped metal segment. These inner rings are also interlinked to the outer ring by using metal strips. Coupling causes to increase the electrical length and modifies the inductance of the unit cell. Multiple resonances covering C, X and Ku-band are achieved due to the interconnection of rings. The symmetric nature of the CCI-SRR unit cell exhibits unique quality to minimize noise and harmonics effect. The unit cell is designed on FR4 substrate with a thickness of 1.6 mm. The overall dimension of the unit cell is $0.124\lambda \times 0.124\lambda$, where λ is the wavelength calculated at a lower resonance frequency of 4.15 GHz. Three resonances are obtained for $|S_{21}|$ at frequencies of 4.15 GHz, 10.38 GHz and 14.93 GHz performing numerical simulation in CST microwave studio. Permittivity, permeability, refractive index and impedance are explored by using the Newton-Ross-Weir (NRW) method. ENG performance is observed in frequencies ranging from 3.95 to 5.65 GHz, 9.57–11.46 GHz, 13.68–16 GHz. Near-zero refractive index is attained within the frequency ranges, 4.16–5.75 GHz, 10.16–11.58 GHz, 14.46–16 GHz. An LC equivalent circuit is designed, and component values are achieved by Advanced Design Software (ADS) justifying $|S_{21}|$ with CST result. The study of electromagnetic wave interaction between the unit cell and the double positive medium reveals that the unit cell exhibits evanescent wave properties. The compact nature of the unit cell is confirmed by calculating EMR with a value of 8.03. The electromagnetic coupling effect is examined for 2×2 array in various orientations. The $|S_{21}|$ performance of 2×2, 4×4 and 8×8 is matched with the unit cell. Due to symmetric patterns, near-zero refractive index, negative permittivity and high EMR, the proposed unit cell can be used to enhance the performance of microwave devices used for C, X and Ku-bands, especially Satellite and Radar communications.

Introduction

Artificial plasmas, negative permeability media, left-handed media are some examples of metamaterials. Artificial plasma displays negative permittivity below plasma frequency. Whereas left-handed media is metamaterial that represents negative permittivity and permeability simultaneously. The exotic characteristics of the metamaterials can be applied for various applications such as for antenna design [1], SAR reduction [2], superlenses [3], filters [4], invisibility cloaking [5], electromagnetic absorber [6], sensors [7], etc. Recently metamaterials are designed by targeting applications in various frequency bands. Because each frequency band has wide applications. Such as C-band covers frequency ranges from 4 to 8 GHz and X-band includes frequencies from 8 to 12 GHz. These two bands are extensively employed for satellite communications. The proposed metamaterial can provide a good platform for the integration in antenna to enhance its technical

* Corresponding authors.
E-mail addresses: p99997@siswa.ukm.edu.my (Md. Moniruzzaman), tariqul@ukm.edu.my (M.T. Islam), mchowdhury@qu.edu.qa (M.E.H. Chowdhury).

https://doi.org/10.1016/j.rinp.2020.103296
Received 10 June 2020; Received in revised form 15 July 2020; Accepted 15 July 2020
Available online 11 August 2020

performance for Satellite and Radar Communications applications. Particularly, numerous GEO satellites are devised to function in C-band. Moreover, for satellite TV, radio communications, this band is also utilized. On the other hand, X-band is applied for RADAR applications for weather monitoring, to control vessels traffic, in defense tracking system etc. Ku-band which is extended from 12 to 18 GHz is vastly used for satellite TV and VSAT in ships. The advantage of the Ku-band is that it is less affected by terrestrial signals and operation in high frequency range allowing to use small sized dish antennas for VSAT application.

Both Single negative (SNG) and double-negative (DNG) metamaterials are extensively designed for various applications. As an earlier work Pendry et al. demonstrated split ring resonator(SRR) based artificial magnetic materials [8], where SRR of different shapes such as circular, rectangular are printed on the dielectric medium. An S-shaped resonator circumference with a ground ring is described in [9]. In this metamaterial, a microstrip line is used for feeding. This material covers L-band with a resonance frequency of 1.8 GHz. A new composite metamaterial for multi-band communication with an EMR of 7.44 is described at [10]. This metamaterial has a dimension of 12 × 12 mm^2 and shows resonances at S, C and X-band. A Greek-key pattern and operates at the frequency range from 1 to 5 GHz designed on a substrate of Rogers RT5880 with a dimension of 10 × 10 mm^2. This metamaterial shows resonances at 2.4 GHz, 3.5 GHz and 4 GHz [11]. A square ring with open delta ENG metamaterial has been proposed in [12]. The proposed metamaterial exhibits three resonances frequencies of 4.32 GHz, 7.55 GHz and 9.76 GHz, which covers C and X-bands. A 3-D spherical shaped metamaterial unit cell is proposed by K. L. Smith et al. with a dimension of 266 × 22 × 22 mm^3. By changing the orientation of the unit cells, negative permeability, negative permittivity or both can be achieved. A combination of negative permeability and negative permittivity cells has been used to get a double negative response [13]. N. Misran et al. has presented a concentric split ring array in [14]. A Mu negative metamaterial has been used to increase directivity and bandwidth of antenna in [15]. An anisotropic metamaterial operating in the frequency range of 30–35 GHz is exercised in [16]. A modified H-shaped metamaterial has been proposed in [17] for X and Ku-band applications. The dimension of the unit cell is 9 × 8.8 mm^2. It provides two major resonances at 9.65 GHz and 12.6 GHz. A hexagonal shaped gap coupled split ring resonator has been proposed by M.S Islam et al. the proposed unit cell covers S and X band with an EMR value of 8.4 [18]. A complementary split ring resonator based metamaterial is presented in [19] which shows its resonance at 7.5 GHz. The dimension of the unit cell is 5 × 5 and provides EMR value of 8. A concentric ring with crossline based single negative metamaterial has been presented by R. Azeez et al. [20]. The metamaterial is constructed on FR4 substrate having dimension of 5 × 5 × 1 mm^3 which shows two resonances at 13.9 GHz and 27.5 GHz. This metamaterial has been utilized to enhance the performance of microstrip transmission line. In [21] double inverted *L* loaded SRR based metamaterial is constructed for C, X and Ku-band applications. Whereas in [22] multi split ring resonators based metamaterial is described for L and S-band applications. A dual band metamaterial has been reported in [23] for absorber applications. This material is composed of elliptical nanodisk graphene with a periodic pattern on a thin SiO_2 dielectric layer. Gold material is used as ground since it acts as good reflector in far infrared frequency domain. A RLC resonator based metamaterial is designed by Eistiak et al. that shows a resonance of 8.84 GHz [24].Another graphene layer based metamaterial absorber presented in [25] where a square-square-circular shaped periodic structure of graphene is used over SiO_2 substrate. A gold layer is sandwiched between this SiO_2 layer and the Si layer. Single negative metamaterial has been used by Maryam Rezapour et al. to reduce the mutual coupling effect of antenna array [26]. In this metamaterial symmetrical split ring resonators is utilized which contains double slots. The inner ring includes an inductive stub. This metamaterial represents two resonances with wider stop bands. Recently, a pie loaded SRR based metamaterial has been presented by R. Islam et al. The dimension of 8 × 8 mm^2 is considered for this design and the metamaterial covers S, C and X-bands [27]. A tunable metamaterial has been presented in [28] consisting of split-ring metal SRR. This metamaterial has the potentiality to reconfigure to eliminate the complexity in case of dynamic filtering, cloaking and sensing. A bilayer chiral metamaterial (CMM) is presented in [29] that exhibits triple-band asymmetric transmission (AT). This metamaterial is composed of two layers of deformed S shaped metallic strips with a dielectric spacer layer. Each asymmetric transmission band of this metamaterial can be triggered adjusting polarization angle of the incident wave. A metamaterial has been explored by Jubaer et. al. where metamaterial shows its transmission stop band at 3.11 GHz [30]. This metamaterial then utilized for developing a band pass filter which can be used for GPS (1.55 GHz), Earth Exploration-Satellite (2.70 GHz) and WiMAX (3.60 GHz) bands of frequencies. In [31] metamaterial based absorber has been presented by A. Hoque et al. that works in X and Ku-bands.

A cross-coupled interlinked split ring resonator (CCI-SRR) based metamaterial is presented in this article for satellite and Radar communications. Metamaterial unit cell design and simulation method is described rigorously in section two. Whereas in section three, electromagnetic and metamaterial property extraction technique is presented. Section four is dedicated on parametric studies on unit cell considering evolution steps of it, effects of splits gaps and substrate materials. Surface current, electric and magnetic field properties are analyzed in section five. Interaction of electromagnetic waves with unit cell and double positive medium is also analyzed in this section. A discussion on equivalent circuit modeling is made in section six. The circuit is designed in ADS, and performance is verified with simulation in CST. The next part of the article focuses on result analysis and discussion about unit cell and array. The investigation is done on transmission & reflection coefficients, effective parameters such as permittivity, permeability, refractive index, impedance. The transmission coefficients ($|S_{21}|$) of the unit cell and array are also validated with measurement results in this section. Parametric analysis of 2 × 2 array is performed and $|S_{21}|$ of 2 × 2, 4 × 4 and 8 × 8 array is analyzed and compared with the unit cell. EMR is calculated, and the performance of the metamaterial is compared with the state of arts.

Unit cell design and simulation

The proposed Cross Coupled Interlinked Split Ring Resonator (CCI-SRR) is designed on the FR4 substrate. The dimension of the substrate material is 9 × 9 × 1.6 mm^3. Conducting copper layers exist on both sides of this substrate with a thickness of 0.035 mm. One side of the substrate is used for constructing the resonator, whereas all copper is removed from the other side of the substrate. As shown in Fig. 1, the proposed unit cell consists of three concentric square shaped rings. The two horizontal sides of the outer ring are splitted in the middle. Two non-split rings are housed inside this outer ring. These two rings are coupled together with a cross shaped striped lines of metal. These two inner rings are also connected to the outer rings by using metal strips. The strip gap is chosen by trial and error basis so that the proposed design provides a maximum number of resonances with higher EMR at each band. All the dimensions of split gaps, metal length and width of rings are described in Table 1. It is noteworthy that all dimensions are selected in such a way that the unit cell is symmetric in any axis. Due to the symmetric nature proposed unit cell will be less affected by noise, and array performance will be better. The performance of the unit cell is checked by simulation, and then it is verified by measurement. Numerical simulation is done by using CST microwave studio. The finite integration technique (FIT) of this software has been utilized for this purpose. Fig. 2 shows the simulation arrangement of the unit cell, where a transverse electromagnetic wave has been applied in the z-axis. Meanwhile, in the x-axis, a perfectly electrical boundary condition is used, and a perfectly magnetic boundary has been used in the y-axis. The simulation process is executed over the frequency range of

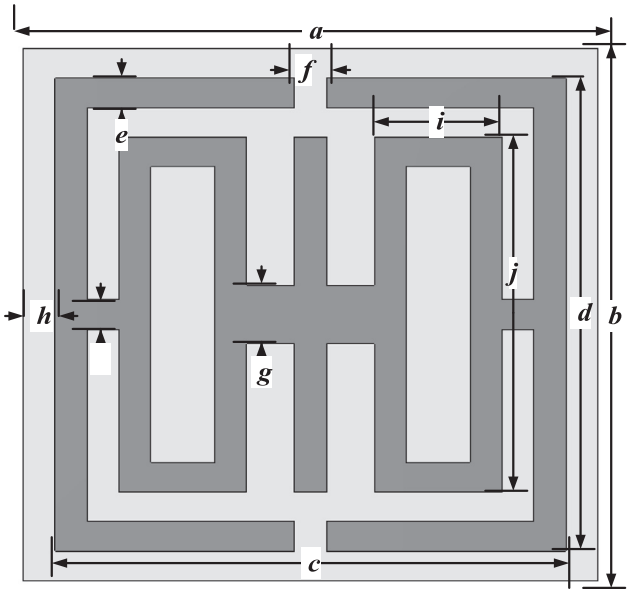

Fig. 1. The layout of the proposed unit cell.

2 GHz–16 GHz.

Electromagnetic field and metamaterial property characterization technique:

The simulation set up presented in Fig. 2 can be represented by the schematic diagram of Fig. 3. Here, an electromagnetic wave is propagating towards the z-axis, conceiving electric and magnetic fields perpendicular to each other. The electric field is acting towards x-axis, whereas the magnetic field works on the y-axis. Before the incident on metamaterial slab, the wave travels through the free space of region 1. In region 2, a portion of the wave is transmitted (forward wave), and a portion is reflected (backward wave) to region 1. The transmitted wave through region 2 comes into the region 3, which is again free space and travels through this medium.

The electric and magnetic fields for these three regions can be presented by using the following equations as introduced in [32]. The phasor of an electric and magnetic field for region 1 is expressed as,

$$E_0 = \left(E_0^t e^{-ik_0 z} + E_0^r e^{-ik_0 z}\right) a_x \tag{1}$$

$$H_0 = \left(H_0^t e^{-ik_0 z} + H_0^r e^{-ik_0 z}\right) a_y \tag{2}$$

Here, E_0^t, E_0^r, $H_0^t = \frac{E_0^t}{Z_0}$, $H_0^r = -\frac{E_0^r}{Z_0}$ are the forward(transmitted) and backward(reflected) electric and magnetic field amplitudes, respectively. $k_0 = \omega\sqrt{\mu_0 \varepsilon_0}$ is the wavenumber of the incident wave and $Z_0 = \omega\sqrt{\mu_0 / \varepsilon_0}$ is the wave impedance in region 1 where μ_0 and ε_0 are permeability and permittivity of the free space. For the metamaterial slab of region 2, phasor form of the electric and magnetic field can be expressed by the equations

$$E_1 = \left(E_1^t e^{-ik_1 z} + E_1^r e^{-ik_1 z}\right) a_x \tag{3}$$

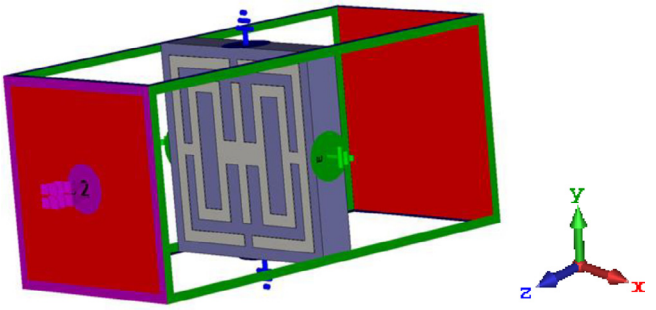

Fig. 2. The simulation setup of the proposed unit cell.

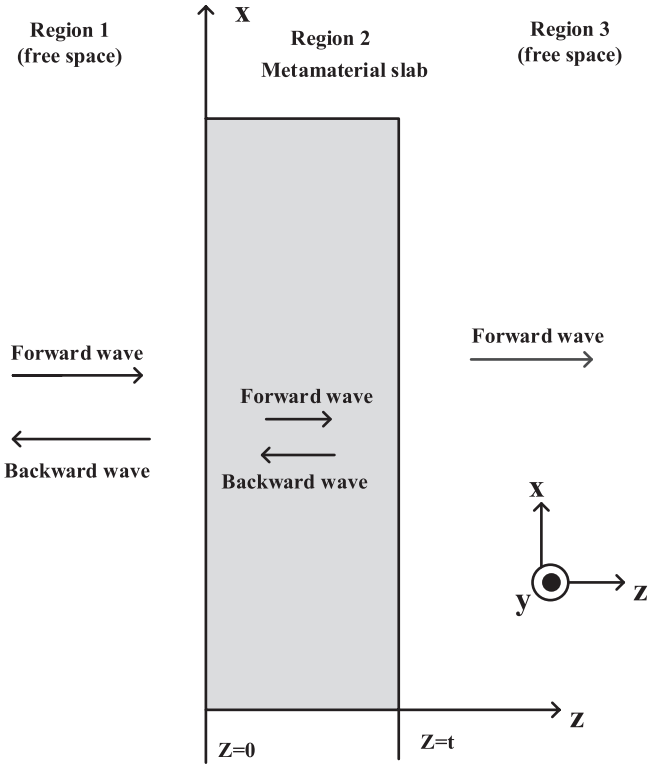

Fig. 3. The normal incidence of the electromagnetic wave on a metamaterial of thickness, t.

$$H_1 = \left(H_1^t e^{-ik_1 z} + H_1^r e^{-ik_1 z}\right) a_y \tag{4}$$

Here, E_1^t, E_1^r, $H_1^t = \frac{E_1^t}{Z_1}$, $H_1^r = -\frac{E_1^r}{Z_1}$ are the forward(transmitted) and backward(reflected) electric and magnetic field amplitudes, respectively. $k_1 = \omega\sqrt{\mu_1 \varepsilon_1}$ is the wavenumber and $Z_1 = \omega\sqrt{\mu_1 / \varepsilon_1}$ is the wave impedance in region 2 where μ_1, ε_1 are the permeability and permittivity of the metamaterial. Similarly, for region 3 phasor form of the electric and magnetic field will be:

$$E_2 = E_2^t e^{-ik_0 z} a_x \tag{5}$$

$$H_2 = H_2^t e^{-ik_0 z} a_y \tag{6}$$

Table 1
Design parameter of the unit cell.

Parameter	Measurement (mm)	Parameter	Measurement (mm)	Parameter	Measurement (mm)
a	9	*e*	0.5	*i*	2
b	9	*f*	0.5	*j*	6
c	8	*g*	1	*k*	0.5
d	8	*h*	0.5	–	–

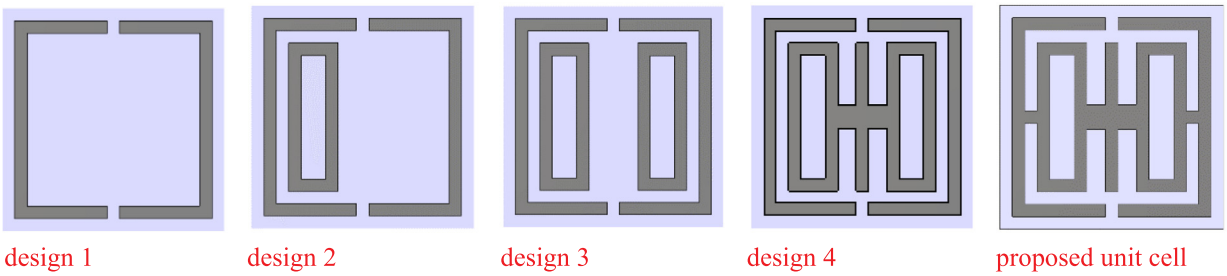

Fig. 4. Design steps of the proposed unit cell.

E_2^t, $H_2^t = \frac{E_2^t}{Z_0}$ are the forwarded(transmitted) electric and magnetic field amplitude in region 3.

By applying boundary condition, for two walls of metamaterial along the z-direction, $z = 0$ and $z = t$ and using normalized wave impedance at metamaterial, $Z = Z_1/Z_0 = \sqrt{\mu_r/\varepsilon_r}$ the relationship between various transmitted and reflected wave with the forward wave of region 1 can be obtained as in [32].

$$E_0^r = \frac{i(Z^2-1)\sin(k_1 t)}{2Z_1 Z_0 \cos(k_1 t) + i(Z^2+1)\sin(k_1 t)} E_0^t \tag{7}$$

$$E_1^t = \frac{(Z^2+Z)e^{-ik_1 t}}{2Z\cos(k_1 t) + i(Z^2+1)\sin(k_1 t)} E_0^t \tag{8}$$

$$E_1^r = \frac{Z_1(Z-Z^2)e^{-ik_1 t}}{2Z\cos(k_1 t) + i(Z^2+1)\sin(k_1 t)} E_0^t \tag{9}$$

$$E_2^t = \frac{2Ze^{-ik_0 t}}{2Z\cos(k_1 t) + i(Z^2+1)\sin(k_1 t)} E_0^t \tag{10}$$

Eqs. (7)–(10) can be used to determine the electric field of various regions of the simulation setup at a particular frequency with known values of permittivity and permeability. Now numerical simulation can be performed to determine the scattering parameters such as transmission coefficient ($|S_{21}|$) and reflection coefficient ($|S_{11}|$) by using CST microwave studio. Various approaches have been practiced in literature such as a robust method [33], Nicolson-Ross-Weir (NRW) method [34,35] to extract the parameters, permeability (μ), permittivity (ε), normalized impedance (z) and refractive index (n).In present work, the popularly used NRW method has been exercised to determine the values of the effective parameters by using the information of $|S_{21}|$ and $|S_{11}|$. Sum and differences of $|S_{21}|$ and $|S_{11}|$ are calculated which can be used for finding out permittivity and permeability.

$$V_1 = |S_{11}| + |S_{21}| \tag{11}$$

$$V_2 = |S_{21}| - |S_{11}| \tag{12}$$

If $X = \frac{1 - V_1 V_2}{V_1 - V_2}$

Then reflection coefficient of the incident wave at the interface,

$$\Gamma = X \pm \sqrt{X^2 - 1} \tag{13}$$

And the transmission coefficient,

$$X = \frac{V_1 - \Gamma}{1 - V_1 \Gamma} \tag{14}$$

The expression for refractive index, n and impedance, z can be derived from these equations. The relative permittivity, ε_r, and relative permeability, μ_r can also be extracted and represented in the form of Eqs. (15) and (16) [36].

$$\varepsilon_r \sim \frac{2}{jk_0 d} \times \frac{(1 - V_1)}{(1 + V_1)} \tag{15}$$

$$\mu_r \sim \frac{2}{jk_0 d} \times \frac{(1 - V_2)}{(1 + V_2)} \tag{16}$$

where $k_0 = \frac{2\pi f}{c}$, c is the velocity of light, and d is the thickness of the substrate.

The expressions are presented for the refractive index, n_r in Eq. (17) and normalized impedance, Z in Eq. (18).

$$n_r = \sqrt{\mu_r \varepsilon_r} \tag{17}$$

$$\text{Normalized impedance, } Z = \sqrt{\mu_r/\varepsilon_r} \tag{18}$$

MATLAB code based on Eqs. (15)–(18) can be utilized to get data related to relative permittivity, relative permeability and refractive index.

Parametric study

The metamaterial unit cell has been designed by utilizing trial and error method. The design criteria for present work are the maximum number of bands covered by the unit cell with reasonable values of $|S_{21}|$, high EMR and Epsilon negative properties. Three different parametric studies have been performed focusing on these design goals. The design procedure undergoes various structural changes to form the proposed unit cell, as presented in Fig. 4. The design is initiated with a single square shaped split ring resonator having a length of 8 mm of each side and a split gap of 0.5 mm at the center of two horizontal sides. For this single ring resonator, a resonance at Ku-band is found, as shown in Fig. 5. In the next step, a rectangular ring has been installed inside the previous ring, as shown in design 2 of Fig. 4. From Fig. 5, it is noticed that the effect of adding a new ring inside the outer one provides an additional resonance at 15.54 GHz. In succeeding step, another extra rectangular ring is added (shown in design 3 of Fig. 4) that helps to increase the magnitude of $|S_{21}|$ with a small change in resonance frequencies. Now, these two rings are added together by using a cross shaped copper connector. It causes to shift the resonance frequency towards lower values. Two resonances occur around 7.9 GHz and 13 GHz that cover C and Ku-bands. The design is completed by adding the inner rings with the outer one, as shown in the proposed unit cell of Fig. 4. This interconnection provides a drastic change in $|S_{21}|$ with three

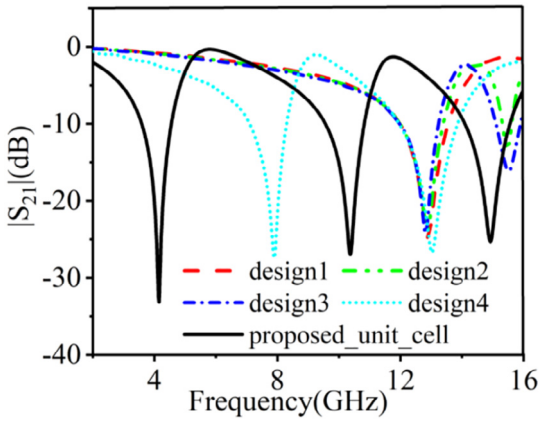

Fig. 5. $|S_{21}|$ for various design steps.

Table 2
$|S_{21}|$ response for various structural change towards the proposed unit cell.

Substructure	Resonance frequency (GHz)	Resonance peak (dB)	Covering bands
design 1	12.9	−24.8	Ku-band
design 2	12.9,15.48	−23.8, −13.4	Ku-band
design 3	12.8,15.5	−24.3, −16.2	Ku-band
design 4	7.9,13	−27.5, −26.7	C-band,Ku-band
proposed unit cell	4.15,10.38,14.93	−35, −26.96, −25.3	C-band, X-band, Ku-band

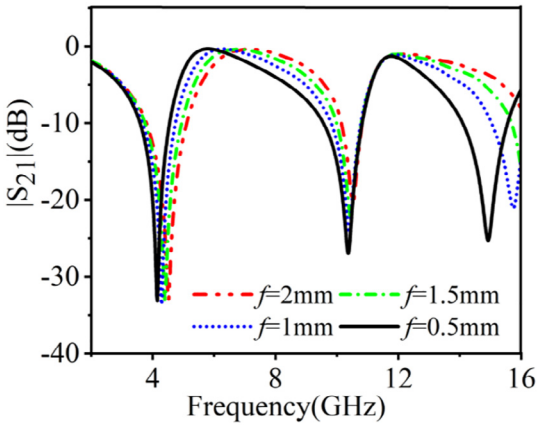

Fig. 6. $|S_{21}|$ for various change of split gap, *f*.

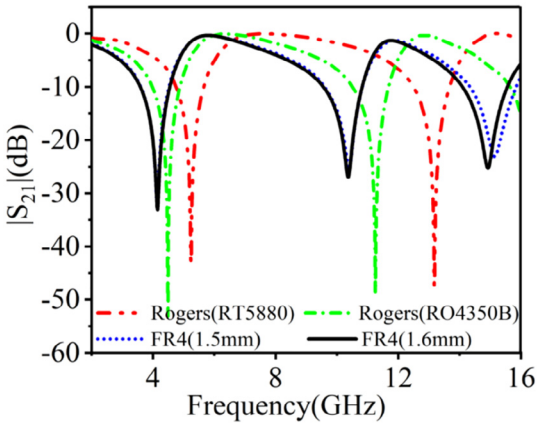

Fig. 7. The change of $|S_{21}|$ with the change of substrate material.

resonances at 4.15 GHz, 10.38 GHz and 14.93 GHz. These resonances cover C, X and Ku-bands. The outcomes for these structural modifications are summarized in Table 2. The effect of changing the split gap on the performance of the proposed unit cell is also studied. In this study, both split gaps of the outer ring have been modified. The $|S_{21}|$ for the various split gaps is presented in Fig. 6. The split gap is changed from 2 mm to 0.5 mm with a step size of 0.5 mm. From Fig. 6, it is noticed that two resonances at C and X-bands occur with a split gap of 2 mm. A shifting of resonance frequency toward lower frequency is noticeable if the split gap decreases gradually. As the split gap decreases, the capacitance due to split increases. The impact of increasing the capacitance is shifting the resonance frequency towards the lower value since resonance frequency, $f = \frac{1}{2\pi\sqrt{LC}}$. When the split gap is 0.5 mm, an additional resonance is observed at 14.93 GHz, thus the proposed unit cell covers C, X and Ku-bands. The effect of changing substrate materials is also studied. In this study, Rogers with two variations and FR-4 with varying thickness are used. In the first observation, Rogers RT 5880, having a thickness of 1.575 mm is applied. The dielectric constant (Dk) of this material is 2.2, and the loss tangent is 0.0004. From Fig. 7, it is observed that this substrate material provides two sharp resonances of $|S_{21}|$ around 5.5 GHz and 13.5 GHz. On the other hand, Rogers (RO4350B) with a thickness of 1.524 mm, Dk = 3.48, loss tangent 0.0037 offers two resonances around 4.5 and 11.5 GHz. Two other studies have been performed by using FR-4 substrate having a thickness of 1.5 mm and 1.6 mm with Dk = 4.4. In the case of thickness 1.5 mm FR-4 substrate three resonances at C, X and Ku-bands are noticed. FR4 with thickness 1.6 mm also covers the same three bands with a shift of resonance at Ku bands. It is noteworthy that the resonance peak for FR4 is lower compared to Rogers. Since FR4 covers maximum bands with higher EMR value proposed unit cell is designed on the FR4 substrate.

Surface current, electric field and magnetic field analysis

The resonant structure proposed in this work contains split gaps and metallic conductors which contribute to capacitive and inductive effects. When a time varying electromagnetic field interact with this unit cell electromagnetic force exerts on the split ring resonator. Due to its small size compared to the wavelength, induced current flows from one ring to other though there is capacitive gap. Induced electric and magnetic moments are created which affect transmission capabilities and material properties such as permeability and permittivity. Fig. 8 represents the surface current distribution of the proposed unit cell. From this figure, it is observed that at the lower resonance frequency of 4.15 GHz, the inner ring contributes a larger amount of current. The inner rings provide a low impedance path since, at low frequencies, inductive reactance will be low. Thus, it shares a big portion of the total current. Two vertical edges of the outer ring contribute a significant amount of current. At point P_1 of Fig. 8(a), external ring currents are accumulated as per the Kirchhoff's current law. This current divides into two parallel paths of left side inner rings following the current divider rule. These currents combine at the junction point indicating by P_2 of the same figure, then the current flows towards the second ring and divides into two parts. Finally, it comes out from the inner ring at point P_3 of Fig. 8(a). Two horizontal sides of the outer ring have less contribution to the currents since it shows larger capacitive reactance due to the split gap at this low frequency. At the resonance frequency of 10.38 GHz, the current density at the middle rings decreases significantly since high frequency causes to increase impedance. At the junction of the two inner rings, current direction alters compared to previous resonance. Through two vertical sides of the left inner ring, two oppositely flowing currents are observed in Fig. 8(b). The horizontal side of these rings acts as sink and current is nearly nullified when these opposite direction currents met. The horizontal side of the right inner ring serves as a source of current. The two currents from the right vertical side meet at the right side junction and flow towards the right side of the outer ring. At this frequency, nonuniform and random movement of current is observed, which ultimately decreases the total current. At 14.93 GHz, it is noteworthy that at area P_4 in Fig. 8(c), the current density is low compared to the left side of the left inner ring and right side of the right inner ring. The direction of the current is fully opposite compared to resonance at 4.15 GHz. Now, the current enters the inner ring from the right side of the unit cell and comes out from the left side of the inner ring. At the two inner sides of inner rings, the current density is less because current cancellation occurs due to oppositely following currents. A comparatively high current flows through the edges of all horizontal sides of all rings. It is observed that two

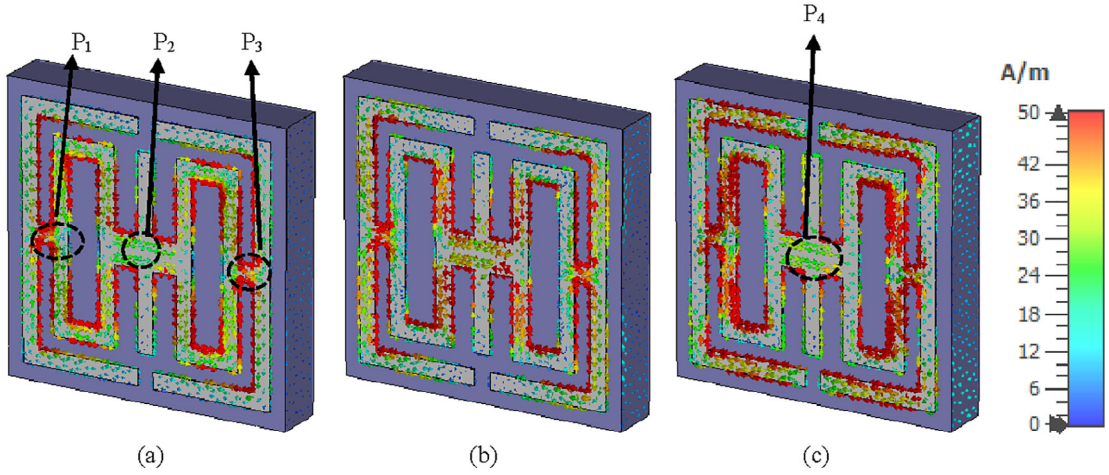

Fig. 8. The surface current distribution of unit cell at three different resonance frequencies (a) 4.15 GHz, (b) 10.38 GHz and (c) 14.93 GHz.

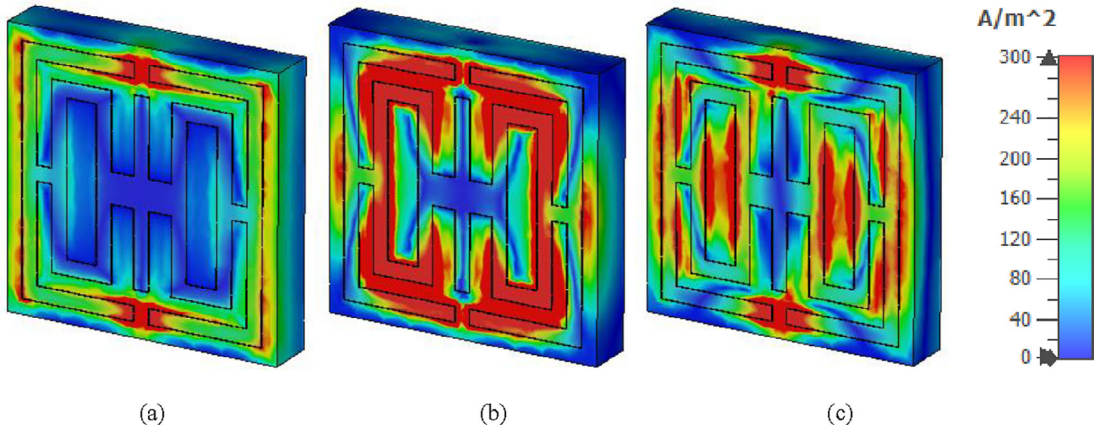

Fig. 9. The current density plot (J-surface) of the unit cell (a) 4.15 GHz, (b) 10.38 GHz (c) 14.93 GHz.

horizontal sides of the outer ring contribute a significant amount of current due to lower impedance exerted by the split gap. The current density plot (J-surface) of the unit cell is displayed in Fig. 9 for three different resonance frequencies. Form Fig. 9, it can be observed that at 4.15 GHz current density is higher over the split gaps and around the outer ring, whereas a denser current is observed in the inner rings and two horizontal sides of the outer ring at 10.38 GHz. Higher current density can also be observed in vertical sides and near the split gaps of the rings at 14.93 GHz.

Time-varying electric charges may cause to generate changing magnetic field as per amperes law which in turn produces electric field due to electromagnetic interaction according to faraday's law. Thus, the electric and magnetic field is coupled together, and the electromagnetic wave is produced. The produced electric and magnetic fields due to time-varying electric charges can be described by Maxwell's curl equations as presented in [37].

$$\nabla \times H = J + \frac{\partial D}{\partial t} \tag{19}$$

$$\nabla \times E = -\frac{\partial B}{\partial t} \quad \text{where,} \quad \nabla = \left[\frac{\partial}{\partial x}, \frac{\partial}{\partial y}, \frac{\partial}{\partial z}\right] \tag{20}$$

Two demonstrate the interaction of these two fields with materials, two more equations are required. This interrelation can be characterized using the following equations as presented in [38].

$$D(t) = \varepsilon(t) * E(t) \tag{21}$$

$$B(t) = \mu(t) * H(t) \tag{22}$$

Both ε and μ in Eqs. (21) and (22) are complex quantities in case of dispersive medium and real for an isotropic lossless material. The values of these two quantities are also frequency dependent. A close observation of surface current and magnetic field, H depicted in Figs. 8 and 10(b) respectively, it is found that the H field has interrelation with the current. As per the amperes law current always induces a magnetic field and its magnitude and polarity depend on the current magnitude and direction. From the surface current analysis, it is noticeable that current density is comparatively high in the inner rings of the unit cell (Fig. 8(a)). From the H field distribution, it is found that the H field is high near the places of high current. H field is near to null at upper and lower edges due to very low current flow at these edges. According to Biot–Savart law, magnetic flux density at a distance r of the conductor, $B = \frac{\mu I}{2\pi r}$, here μ is the permeability of the medium. So, the magnetic field becomes weaker as the distance from the metal conductor increases. In the middle of the unit cell (marked with red circles in Fig. 10(b)), magnetic field approaches to zero, since these places are far from the current conducting surface. By comparing E field and H field pattern presented in Fig. 10(a) and (b), it is noticed that E decreases if the rate of change of the H field is positive. E field intensity is observed progressively high in case of the negative rate of change of H field. E and H field pattern supports the relation presented in Eqs. (19) and (20). In case of constant H field (near the center of cross coupling point in Fig. 10(b)) E field is nullified as displayed in Fig. 10(a).

The interaction of the electromagnetic wave with different media is investigated by placing the proposed unit cell in between two double positive media (DPS) as depicted in Fig. 11. The DPS is constructed considering the dimension equal to the unit cell. Epoxy resin is used as a

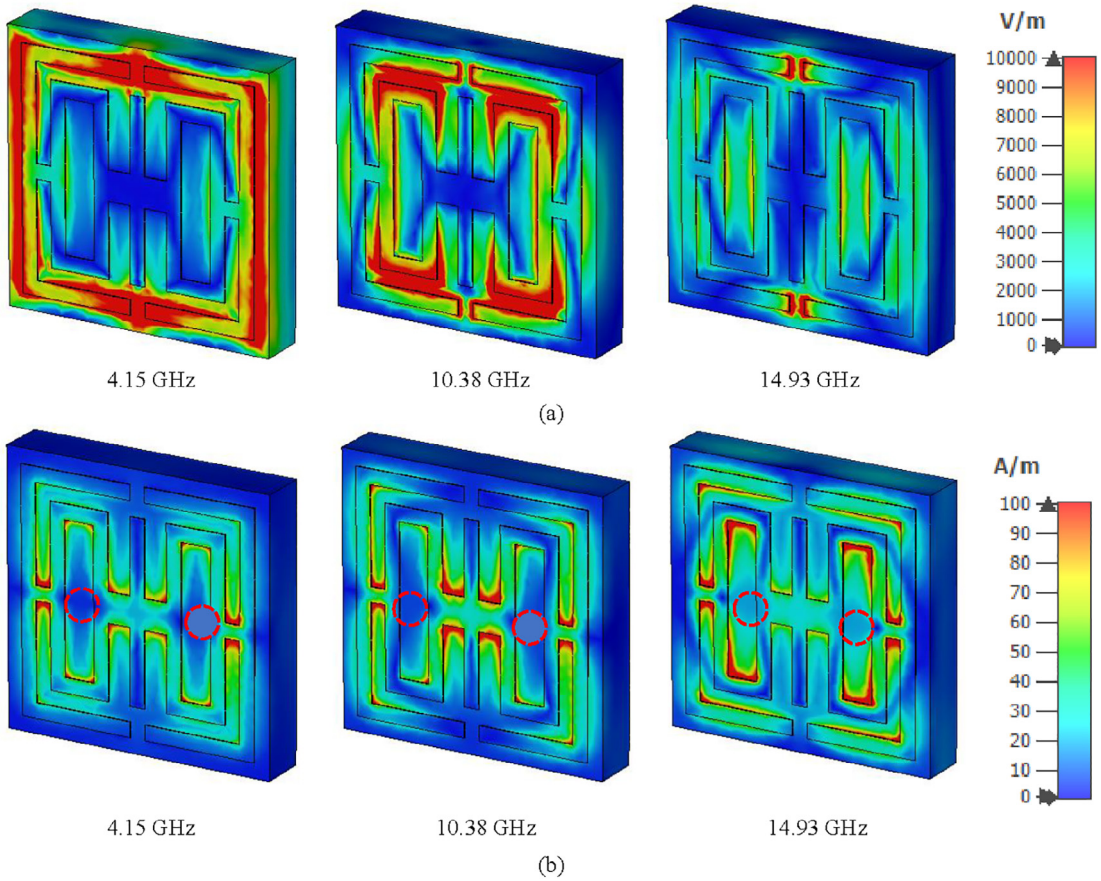

Fig. 10. (a) E field distribution, (b) H field distribution of the proposed unit cell.

DPS with permittivity 4.3 and permeability 1.0. An electromagnetic wave propagating in the z-direction is applied whose electric field acts along the x-axis and magnetic field in the y-axis. In Fig. 12, electric field distribution for this interactive medium is presented for three different resonance frequencies. This figure illustrates that the electric field is mostly concentrated within the ENG medium with a little spreading in the DPS medium. As the distance from the ENG material increases E field gradually feds away. A comparison of the E field between front and backside of ENG medium convinces that wave existed in evanescent decaying states. The field strength in the backside is very low compared to the front side of ENG metamaterial.

Equivalent circuit modelling:

The proposed metamaterial consists of inductive and capacitive elements that resemble an LC resonance circuit. The resonance frequency(f) of this circuit can be calculated by using Eq. (23) as given in [39].

$$f = \frac{1}{2\pi\sqrt{LC}} \tag{23}$$

where L and C denote inductance and capacitance of the structure, respectively. In the unit cell, metal strips of the structure form the inductance and the splits in the structure are the sources of capacitance. The quasi-state theory gives the capacitance between the distances or splits as below:

$$C = \varepsilon_0\varepsilon_r\frac{A}{d}(F) \tag{24}$$

Here, $\varepsilon_0$is the permittivity in free space and ε_r is the relative permittivity, A is the split conducting strip and d is the split distance. The equivalent inductance can be calculated by using the equation based on the principle of transmission line [31]

$$L(nH) = 2\times10^{-4}l\left[\ln\left(\frac{l}{w+t}\right) + 1.193 + 0.02235\left(\frac{w+t}{l}\right)\right]K_g \tag{25}$$

Here K_g is the correction factor, and$K_g = 0.57 - 0.145\ln\frac{w'}{h}$, where w'

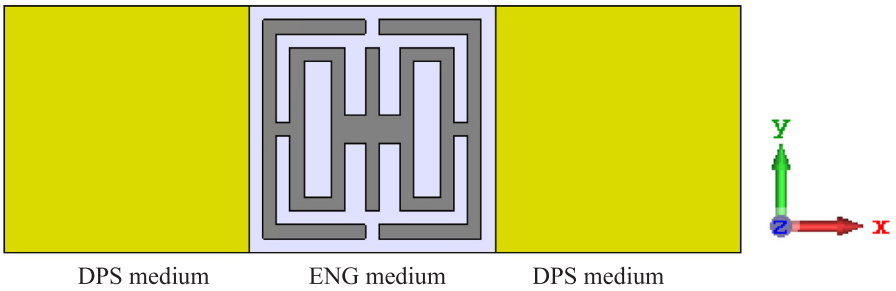

Fig. 11. The numerical model used to study electromagnetic wave interaction between DPS and ENG medium.

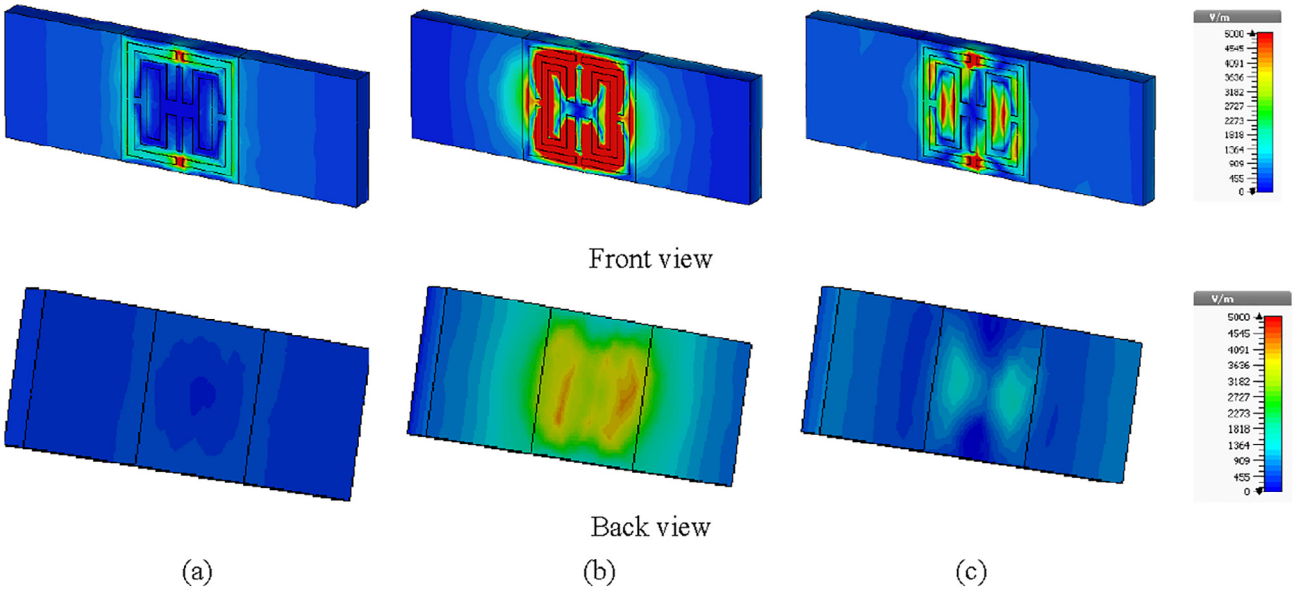

Fig. 12. Numerically computed E field distribution for DPS-ENG-DPS medium (a) 4.15 GHz (b) 10.38 GHz (c) 14.93 GHz.

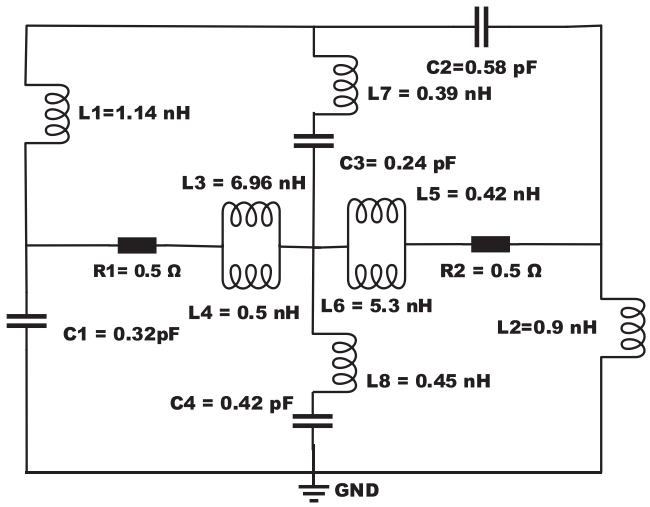

Fig. 13. Equivalent circuit of the unit cell.

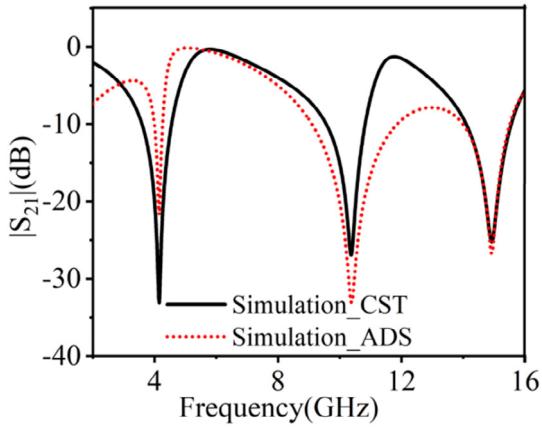

Fig. 14. The simulated waveform of unit cell extracted using CST software and equivalent circuit using ADS.

is the width and h is the substrate thickness. Also, t is the microstrip line thickness, l is the length, and w is the microstrip line width. An approximated equivalent circuit is presented in Fig. 13 for the proposed unit cell. In the circuit *L1, L2, L3, L4, L5, L6*, represent different inductors caused by strip lines, whereas *C1*, *C2*, represent different capacitors due to the split gaps. The values of inductance and capacitance have been optimized by using advanced design system (ADS) simulation tools. In the circuit, *L1* & *C1* contribute to the resonance at 4.15 GHz where *L1* controls the resonance frequency of $|S_{21}|$ whereas *C1* is the influential factor for modifying the magnitude. *L3* and *L4* are the two parallel inductors that representing one rectangular non-splitting ring whereas inductor pair *L5*, *L6* is for another rectangular non-splitting ring in the middle of the unit cell. Proper adjusting of these inductances is necessary as these inductors show a significant influence on all the resonances of 4.15 GHz, 10.38 GHz and 14.92 GHz. Similarly, *L2, C2* represents strip line inductor and split capacitor for the right half of the outer split ring. These quantities show their influence on all the resonance frequencies as all the rings are connected. *C3, C4* are the coupling capacitors and *L7, L8* are inductors for the extended conductors in the middle of the cell. It is observed by the ADS simulation that *C4* and *L8* show their dominant influence on adjusting the resonance frequency of 10.38 GHz, whereas *C3* and *L7* show its impact on resonances at 10.93 GHz. The coupling of different rings is presented by inductors *L6* and *L7*. It is noteworthy that the resistances *R1* and *R2* which are considered the equivalent resistances of the unit cell act as regulators which control $|S_{21}|$ at resonance frequencies and the magnitude of $|S_{21}|$ at stopbands. These resistances are adjusted to get the resultant waveform of Fig. 14. A comparison of simulated $|S_{21}|$ obtained from ADS and CST is shown in Fig. 14. A close similarity between these two $|S_{21}|$ curves is identified form this figure.

The input impedance of the equivalent circuit of Fig. 13 can be obtained by applying Thevenin theorem from the input terminal. To apply this method lumped components of each branch of the Fig. 13 have been represented by the corresponding impedances where $\mathbf{Z_1}$ = jωL1, $\mathbf{Z_2}$ = jωL7 + 1/jωC3, $\mathbf{Z_3}$ = 1/jωC2, $\mathbf{Z_4}$ = R1 + jω (L3 || L4), $\mathbf{Z_5}$ = R2 + jω(L6 || L6), $\mathbf{Z_6}$ = 1/jωC1, $\mathbf{Z_7}$ = jωL8 + 1/jωC4, $\mathbf{Z_8}$ = jωL8. Step1 of Fig. 15 shows the modified form of the circuit of Fig. 13. Circuit presented in this figure contains several delta connected branches. Within this ΔABC is converted to corresponding Y and modified circuit is presented in step 2 of Fig. 15. In step 3 of Fig. 15, two series impedances, ZB & Z3 are combined. Now, ΔCDE is converted to Y and circuit is redrawn in step 4 of the Fig. 15. For brevity, Δ-Y conversion method is omitted here. Now, input impedance can be expressed by using the following expression.

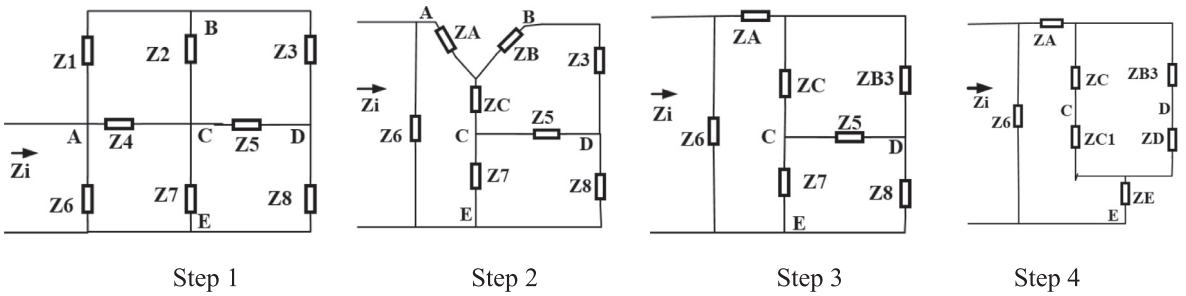

Fig. 15. Different steps to determine the input impedance expression.

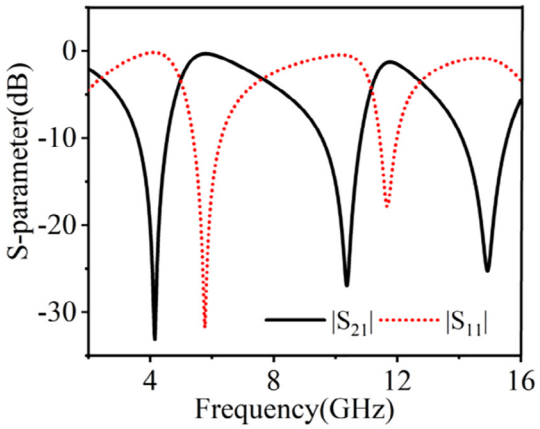

Fig. 16. Simulated S-parameter of the proposed CCI-SRR.

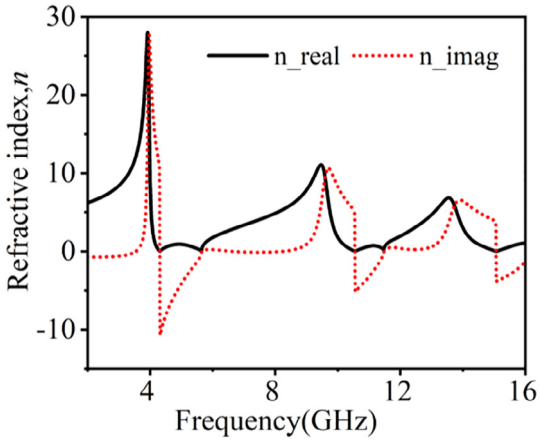

Fig. 18. Refractive index plot of CCI-SRR.

Table 3
Extracted data of the proposed unit cell.

Parameter	Frequency Range(GHz)	Extracted property
Transmission coefficient($\|S_{21}\|$)	3.6–4.7, 9.6–10.8, 14.1–15.5	$\|S_{21}\| < -10$ dB
Permittivity, ϵ_r	3.95–5.65, 9.57–11.46, 13.68–16	ϵ_r less than 0
Refractive index, n	4.16–5.75,10.16–11.58,14.46–16	$n \sim 0$

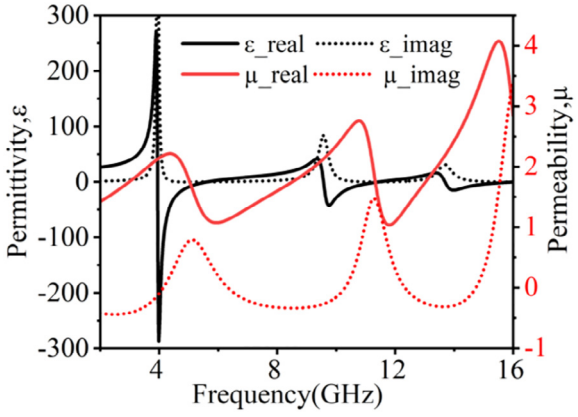

Fig. 17. Permittivity and permeability graph of proposed CCI-SRR.

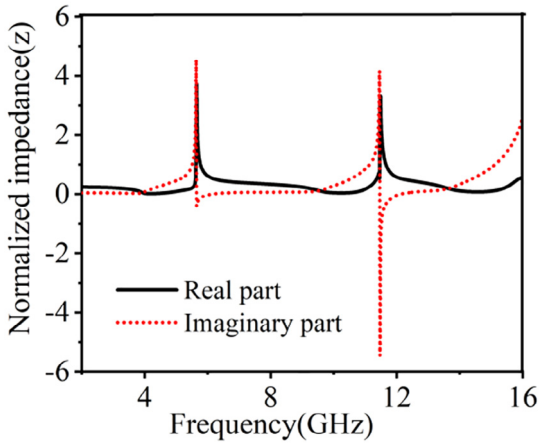

Fig. 19. Normalized impedance graph of CCI-SRR.

$$\mathbf{Z_i} = \mathbf{Z_6}||[\mathbf{Z_A} + \{(\mathbf{Z_C} + \mathbf{Z_{C1}})||(\mathbf{Z_{B3}} + \mathbf{Z_D})\} + \mathbf{Z_E}] \quad (26)$$

The impedances for the circuit presented in Fig. 13 are obtained by using ADS that provides impedance, $Z = Z_0*(0.815 + j0.015)$ at 4.15 GHz, $Z = Z_0*(1.033 + j0.024)$ at 1038 GHz and $Z = Z_0*(0.991 + j0.012)$ at 14.93 GHz where Z_0 is the characteristics impedance.

Result and discussion

The numerical simulation method in CST is applied to obtain the S parameters of the proposed unit cell and the transmission coefficient ($|S_{21}|$) and reflection coefficient($|S_{11}|$) are illustrated in Fig. 16. The unit cell exhibits three resonances of S_{21} at frequencies of 4.15 GHz, 10.38 GHz and 14.93 GHz with an amplitude of −33 dB, −26.96 dB and −25.2 dB, respectively. On the other hand the reflection coefficient, $|S_{11}|$ shows its negative peak at 5.77 GHz and 11.67 GHz with an amplitude of −33 dB and −25.2 dB. A bandwidth of 0.96 GHz at C-band, 1.28 GHz at X band and 1.42 GHz at Ku-band are obtained from the resonances. The data regarding S-parameters, permittivity, permeability, and refractive index are also presented in Table 3. Permittivity, permeability and refractive index are extracted from MATLAB code by using the NRW method. From Fig. 16, it is observed that each resonance

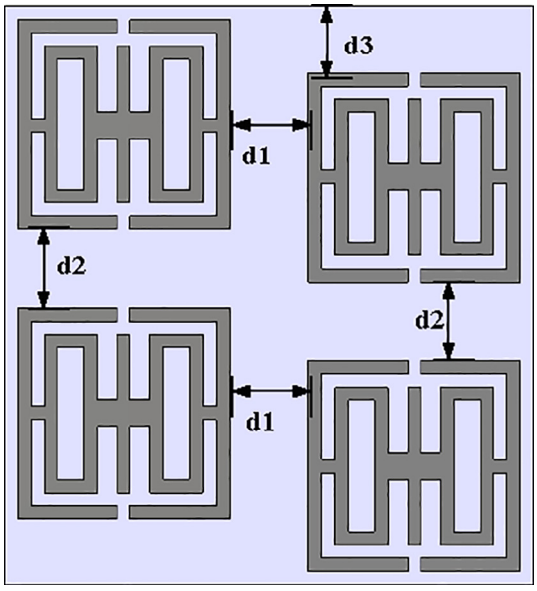

Fig. 20. Irregular arrangement of 2 × 2 array.

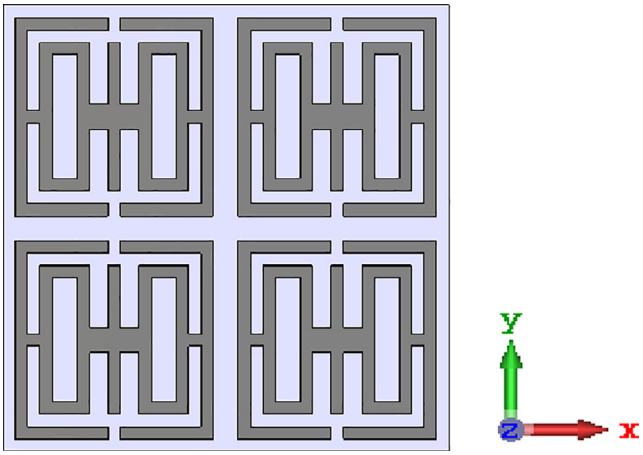

Fig. 21. Regular arrangement of 2 × 2 array.

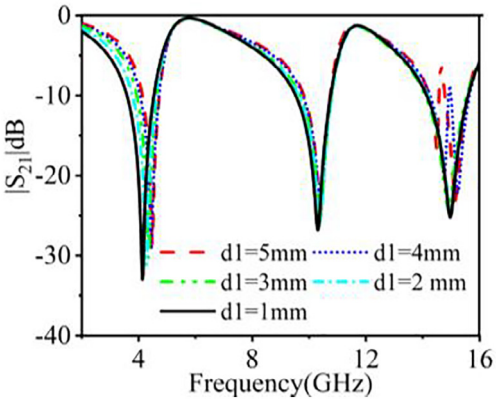

Fig. 22. $|S_{21}|$ response of 2 × 2 array for change of d1 with d2 = 1 mm, d3 = 0.5 mm.

of $|S_{21}|$ is followed by a $|S_{11}|$ minimum. Since the frequency of every $|S_{21}|$ minimum is always lower than the corresponding $|S_{11}|$ minimum frequency so, every resonance can be considered as electrical resonance in the unit cell [40]. Permittivity and permeability graphs are presented in Fig. 17 whereas the graph of refractive index and normalized

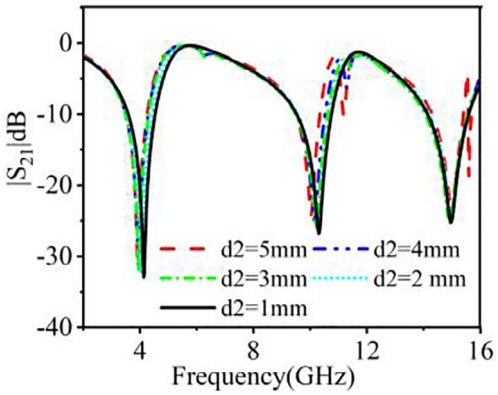

Fig. 23. $|s_{21}|$ for 2 × 2 array for change of d2 with d1 = 1 mm, d3 = 0.5 mm.

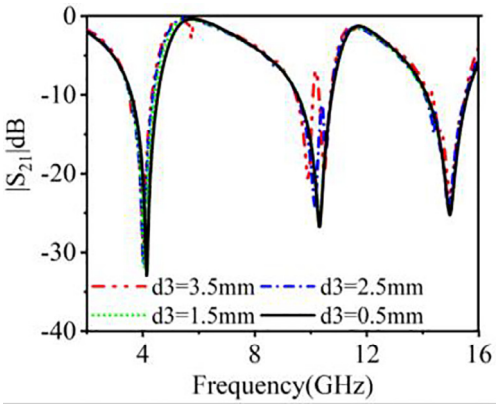

Fig. 24. $|s_{21}|$ for 2 × 2 array for change of d3 at d1 = 1 mm and d2 = 1 mm.

impedance is depicted in Figs. 18 and 19. From Fig. 17, it is noticed that permittivity undergoes form maximum value to minimum value when resonance occurs in $|S_{21}|$. It is also observed from the same figure that the minimum value of permeability is obtained at the places where $|S_{11}|$ is minimum. The permittivity undergoes in the transition from positive to negative whereas permeability is positively changing quantity. From Fig. 18, it is noticed that the refractive index is a function of frequency and it exhibits near-zero property at ENG region. Since permittivity of the proposed unit cell becomes negative in a certain frequency range so, this material is called ENG metamaterial. The negative permittivity can also be explained by using the Drude function [41]:

$$\varepsilon(\omega) = 1 - \frac{\omega_p^2}{\omega(\omega + i\Gamma)} \tag{27}$$

Here, Γ is the damping factor due to which energy dissipates in the plasmons and ω_p represents plasmon frequency. Plasma frequency, $\omega_p = \frac{dq^2}{\epsilon_0 m}$ where d, q, ϵ_0, m are the effective density, electron charge, permittivity of free space and mass of electron respectively. If losses are neglected ($\Gamma \approx 0$) then when $\omega < \omega_p$, permittivity will be negative. In that case, the wave can not be propagated. Form this equation, it will also be observed that the refractive index, n_r will be imaginary and in this media, the wave will be evanescent. It is evident from Fig. 18 that in the negative permittivity region, the refractive index is almost imaginary. Negative permittivity property can be used to various applications in the communication sector such as for bandwidth enhancement of antenna [42], microwave filter design etc. On the other hand, the near-zero refractive property has been utilized for various purposes in communication sectors such as to enhance antenna gain [43,44] and directivity [45]. A close investigation of normalized impedance in Fig. 19 represents that both real and imaginary part of the impedance is positive in the frequency bands where metamaterial shows ENG

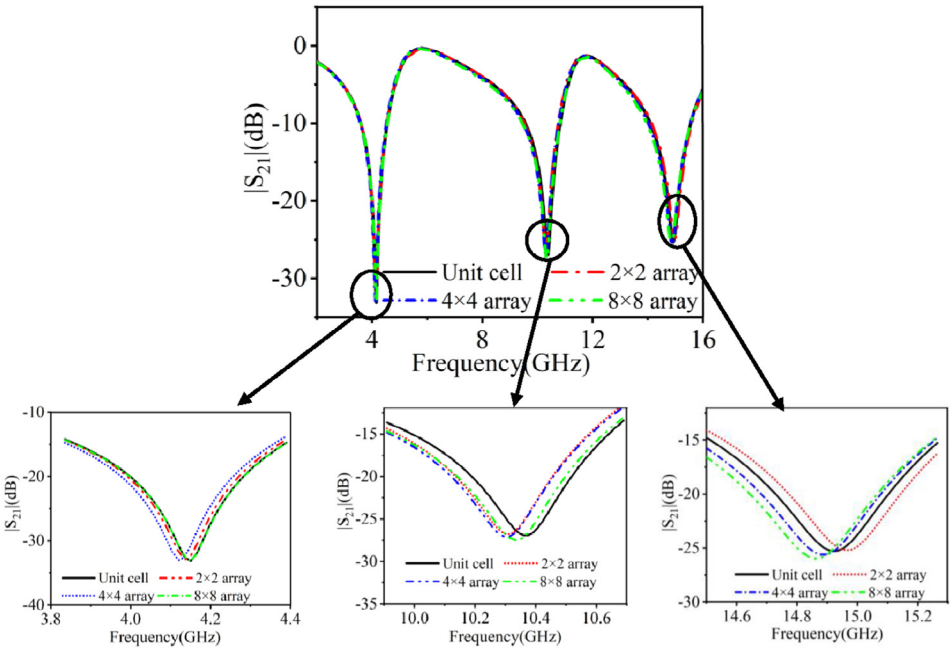

Fig. 25. $|S_{21}|$ comparison for unit cell and different array structure.

Table 4
Comparison of resonance frequency, bandwidth and percentage shift of resonance among unit cell, 2 × 2, 4 × 4 and 8 × 8 array of unit cells.

Parameter	Unit cell (GHz)	2 × 2 array (GHz)	4 × 4 array (GHz)	8 × 8 array (GHz)	Max shift of Resonance (%)
1st Resonance & bandwidth	4.15 0.96	4.14 0.95	4.12 0.95	4.15 0.96	0.72
2nd resonance & bandwidth	10.38 1.26	10.32 1.22	10.3 1.2	10.33 1.36	0.58
3rd resonance & bandwidth	14.92 1.47	14.97 1.45	14.89 1.52	14.86 1.59	0.4

characteristics. Since the real and imaginary component is positive so, metamaterial acts as a passive component [46].

Array metamaterial results

In many practical situations, the metamaterial unit cell does not work independently. In that case, the array of unit cells is utilized to manifest attractive electromagnetic properties of metamaterial. Due to this reason, the performance of the metamaterial array is required to investigate. To observe the coupling effect among unit cells for various arrangements in an array, a parametric study has been executed on 2 × 2 array elements to obtain a better arrangement that provides $|S_{21}|$ response similar to the unit cell. As presented in Fig. 20, d1 represents column distance among the unit cells in the array, d2 is the distance between two rows and d3 is the length between the top edge of the substrate and the first cell of the second column of the array. The simulation arrangement for this study is the same as presented in Fig. 2. In this parametric study, $|S_{21}|$ is considered a function of a single variable of d1, d2 and d3 keeping others constant. The change of $|S_{21}|$ with the variation of d1 is observed for fixed d2 = 1 mm and d3 = 0.5 mm. $|S_{21}|$ response is illustrated in Fig. 22 for every 1 mm change of d1 from 1 to 5 mm. By investing in the graph of Fig. 22, it is observed that when d1 is 5 mm and 4 mm higher order harmonics are observed around 15 GHz. At this distance, low and mid frequency resonances are shifted towards high frequency compared to the other distances though the shift is nominal. Within d1 values of 1 to 3 mm, the high frequency harmonics are eliminated and as the distance d1 decreases, mid and high frequency shifts towards lower values. As the distance d1 increases the separation between unit cells of two columns

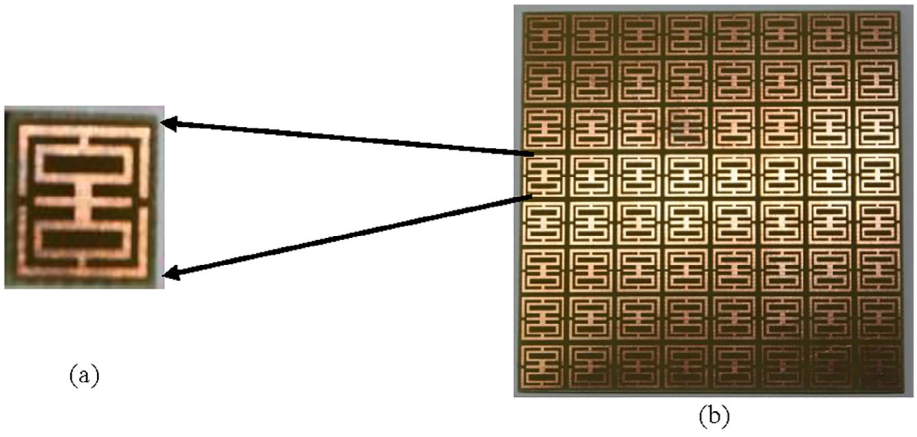

Fig. 26. (a) Fabricated unit cell, (b) 8 × 8 array of the unit cells.

(a) (b)

Fig. 27. (a) Measurement set up for evaluating performance of unit cell (b) measurement set up for array.

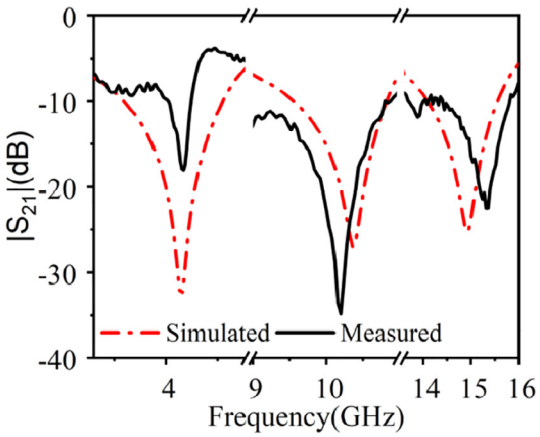

Fig. 28. Transmission coefficient comparison between measured and simulation results of the unit cell.

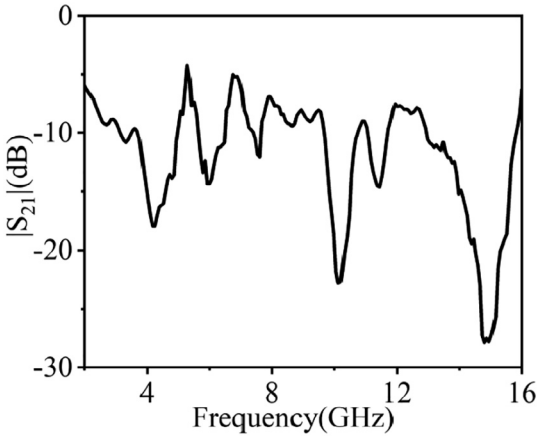

Fig. 29. The measured transmission coefficient of array.

rises thus it decreases the values of coupling capacitors. The decreased values of capacitance cause to increase the resonance frequency. When d1 > 3 mm, electrical coupling between two consecutive column cells decreases whereas magnetic coupling is constant. Due to the change of this electromagnetic effect, high frequency harmonics may initiate. Now, to investigate the effect of changing magnetic induction between two consecutive cells between two rows, d2 is varied keeping d1 and d2 fixed at 1 mm and 0.5 mm respectively. Unlike the previous result, when d2 increases from 1 to 5 mm low and mid resonance frequency shift towards lower values as shown in Fig. 23. In the case of d2 = 4 mm a harmonic at frequency 11.5 GHz is observed. When d2 = 5 mm, the amplitude of this harmonic increases with an additional harmonic at 15.5 GHz. The occurrence of this extra resonance can be explained as the d2 increases, the separation between consecutive unit cells of two rows also increases. This increasing distance may affect magnetic coupling and modifies the inductance and capacitance of the array structure. This change effects $|S_{21}|$ response. Fig. 24 represents the transmission coefficient plot for the change of d3 keeping d1 and d2 constant at 1 mm. The effect of harmonics is pronounced when d3 is greater than 0.5 mm. it is due to the nonuniformity of alignment of the array elements compared to first column elements. Thus, cross coupling effect is more noticeable as d3 changes from the regular orientation. From this study, it is vindicated that inter cell distance of 1 mm and edge distance of 0.5 mm between substrate and unit cell offers the same response of the unit cell. So, the orientation of unit cells of Fig. 21 is considered as a regular arrangement of 2 × 2 array with d1 = d2 = 1 mm and d3 = 0.5 mm. This uniform orientation provides sufficient coupling among the unit cells to exhibit similar $|S_{21}|$ response of the unit cell.

The 4 × 4 and 8 × 8 arrays of the proposed unit cell are also formed in a similar pattern of 2 × 2 array. The transmission coefficient of these arrays is compared with the transmission coefficient of the unit cell as presented in Fig. 25. The array arrangement shows the similar triple band characteristics with a small variation in the resonance frequency and bandwidth at each frequency band. The variation is illustrated in Table 4. From this table, it is observed that at first resonance, unit cell and 8 × 8 array show their resonance at 4.15 GHz with the same bandwidth whereas 2 × 2 and 4 × 4 show their resonances around 4.14 GHz and 4.12 GHz respectively with a bandwidth of 0.9 GHz. For the second and third resonance, the change of the resonance frequency and bandwidth is also negligible. In all cases, the variation of the resonance frequency is less than 1% which indicates that array and unit cell shows nearly the same performance. The symmetric nature of the rings and splits helps to achieve this performance. Due to the symmetric pattern of unit cell construction, mutual coupling and induced effect of the magnetic field are less pronounced. Thus, the transmission coefficient is not affected by harmonics and displays nearly the same scattering behavior and electromagnetic properties all over the frequency spectrum.

Experimental results and discussions

To investigate the validation of the simulation result, the experimental arrangement has been set up by fabricating the unit cell and its 8 × 8 array. The experiment for the unit cell is conducted by placing the unit cell in the middle of two waveguide ports. The waveguide ports are connected to the Agilent N5227A vector network analyzer. The unit cell prototype and experimental set up are represented in Figs. 26(a) and 27(a) respectively. The experimental findings of the transmission coefficient are compared with the finds of simulation as displayed in Fig. 28. The experimental output confirms the similar triple bands those

Table 5
Comparison of the proposed unit cell with another state of arts (comparison is made based on dimension, resonance frequencies, covering bands EMR).

Reference	Year	Shape	Dimension Physical (mm × mm), Electrical (λ × λ)	Resonance Frequency (GHz)	Frequency band	EMR
[9]	2016	S shape	35 × 35, 0.21λ × 0.21λ	1.8 GHz	L	4.76
[10]	2017	Double C shape	12 × 12, 0.134λ × 0.134λ	3.36,8.58,11.57	S, C, X	7.44
[12]	2017	Open delta loop	6 × 6, 0.086λ × 0.086λ	4.32,7.55,9.76	C, X	11.5
[17]	2018	Modified H	9 × 8.8, 0.125λ × 0.125λ	9.65,12.6	X, Ku	3.45
[18]	2020	Hexagonal SRR	10 × 10 0.33λ × 0.33λ	3.57,11.6	S,X	8.4
[19]	2019	CSRR	5 × 5, 0.161λ × 0.161λ	7.5	C	8
[20]	2017	Concentric Ring	5 × 5, 0.232λ × 0.232λ	13.9,27.5	Ku, K	4.4
[21]	2019	Inverse Double L	10 × 10 0.26λ × 0.26λ	7.69, 8.46, 13.12, 14.03	C-, X-, Ku	3.9, 3.55, 2.89, 2.14
[24]	2019	RLC	10 × 8 0.29λ × 0.24λ	8.84	X	3.39
[28]	2015	SRR	5 × 5, 0.17 × 0.17λ	10.2	X	5.88
[47]	2020	CSR	8 × 8, 0.15λ × 0.15λ	5.80, 16.61	C	6.47
[48]	2016	Z shape	10 × 10, 0.252λ × 0.252λ	7.57,12.02	C, X	3.96
Proposed unit cell	2020	CCI-SRR	9 × 9, 0.124λ × 0.124λ	4.15, 10.84,14.93	C, X, Ku	8.03

cover C, X, Ku-bands. It is also noticeable that the experimental result conceives some amount of noise and harmonics. Moreover, second and third resonance frequencies are a little bit shifted though they both have close similarities. Several factors may be the reason for this mismatching. Fabrication error during manufacturing may cause to affect the performance of the unit cell. The experimental setup is also a limiting factor because the proper alignment of the unit cell between two waveguide ports is very important to get the desired performance. These mismatches will be compensated by shifting resonances. Network Analyzer needs to be calibrated properly otherwise calibration error may superimpose with the experimented results. Two waveguide ports also introduce mutual coupling which stipulates additional signal as noise during measurement. Due to the cumulative effect of all these limitations, experimental output exhibits a little shift of resonance frequencies with harmonics. Fig. 26(b) shows a fabricated array prototype of dimension 72 × 72 mm^2 containing a total of 64 unit cells in a square matrix array. The performance is measured through the experimental setup arrangement shown in Fig. 27(b). In this experimental procedure, two horn antennas are used for transmitting and receiving of electromagnetic waves. The two antennas are placed at a distance around 50 cm to avoid near field radiation. At the bisection point of this distance, the array element is placed. The terminals of the antenna are connected to a vector network analyzer by using a long cable. The complete experiment is accomplished in an anechoic chamber so that external noise cannot obstruct the performance of the array. The performance of the array element is evaluated by observing the transmission coefficient spectrum. Fig. 29 depicts the $|S_{21}|$ of the array element. A close observation of this figure reveals that the array exhibits similar triple band characteristics as unit cells. It is also visible from this figure that array shows harmonics at mid frequencies. There are small differences among the resonance frequencies compared to simulation results. Again, fabrication tolerance may affect the performance of array performance. Measured plot exhibits some amount of noise which may be generated by the long extending cable from network analyzer to horn antenna However, the proposed C, X and Ku-bands are achieved by this the array prototype.

The compactness of the proposed unit cell is investigated by calculating the effective medium ratio (EMR). The effective medium ratio is the ratio of wavelength to the maximum dimension of the unit cell and can be express by the equation, $EMR = \lambda/L$. Here wavelength, λ is calculated at the lowest resonance frequency and L is the length of CCI-SRR unit cell. At the lower resonance frequency of 4.15 GHz, the EMR of the unit cell is 8.03. This high EMR value help to improve the homogeneity of the proposed unit cell. It also shrinks the electrical size without compromising the fabrication limit. A comparison has been accomplished between the proposed unit cell and other states of arts based on the electrical and physical dimension, resonance frequency, EMR and frequency bands of application as presented in Table 5. From the table, it is observed that [12] exhibits higher EMR compared to the proposed unit cell within its smaller dimension of 6 × 6 mm^2 but it covers only C and X-bands. Similarly [19,20,28,47] has a lower physical dimension but single band coverage and lower EMR are two major constraints of these designs. Proposed CCI-SRR metamaterial covers maximum of three frequency bands with a moderate EMR value and physical dimension compared to other states of arts stated in Table 5.

Conclusion

A cross-coupled interlinked split ring resonator (CCI-SRR) based tri-band epsilon negative metamaterial has been designed and analyzed in this paper. The unit cell is designed on an FR-4 substrate with an electrical dimension of 0.124λ × 0.124λ at 4.15 GHz. The designed unit cell is simulated in CST and fabricated. Simulated and measured $|S_{21}|$ exhibit tri-band response covering C, X and Ku-bands. Important parameters such as permittivity, permeability, refractive index and normalized impedance have been extracted by using popularly used NRW method and results provide negative permittivity with the near-zero refractive index. Extensive analysis has been performed on the surface current, electric and magnetic field. The electromagnetic wave interaction between DPS-ENG media is investigated. The result exhibits that most of the incident wave is concentrated in the ENG medium, and it represents evanescent wave properties. The electromagnetic coupling effect is studied among the array elements by changing the orientation of array elements in the 2 × 2 array. Through this study, a suitable arrangement of array elements has been selected so that array exhibits the same response of unit cell without affecting by harmonics. Thus, the

performances of 2 × 2, 4 × 4 and 8 × 8 array have been analyzed those show good agreement with the unit cell. The equivalent circuit of the proposed unit cell is designed, and performance is verified through ADS. $|S_{21}|$ response of this equivalent circuit is closely related to CST simulation result. The proposed unit cell provides an EMR of 8.03 at the resonance frequency of 4.15 GHz that ensures a compact dimension satisfying metamaterial's criteria of length, $L < \lambda/4$. Due to small dimensions, near-zero refractive index and negative permittivity properties proposed unit cell can be used to enhance performance for various devices of microwave frequencies such as in antenna, bandpass filter, EM cloaking operations etc. Since C, X and Ku-bands are mostly used for satellite and Radar applications so proposed unit cell may be a good candidate to enhance the performance of Satellite and Radar application devices.

Funding

The project was funded by the Deanship of Scientific Research (DSR), King Abdulaziz University, Jeddah, Saudi Arabia under grant no. KEP-24–135-38. The authors, therefore, acknowledge with thanks DSR technical and financial support. Also, it was made possible by NPRP12S-0227–190164 from the Qatar National Research Fund, a member of Qatar Foundation, Doha, Qatar. The statements made herein are solely the responsibility of the authors. The author also like to thanks Universiti Kebangsaan Malaysia research grant code: KK-2020-005.

CRediT authorship contribution statement

Md. Moniruzzaman: Conception, Design, Result analysis, Planning, Measurement, preparation and revision of manuscript. **Mohammad Tariqul Islam:** Supervision, Experimental work, result investigation, Funding acquisition, revising the article. **Md. Tarikul Islam:** Conception, Design, Result investigation, Planning, Measurement, preparation and revision of manuscript. **Muhammad E.H. Chowdhury:** Result investigation, Funding and revising the article. **Hatem Rmili:** Result investigation, funding and revising the article. **Md. Samsuzzaman:** Conception, Design, Result investigation, Measurement and Writing - Reviewing and Editing.

Declaration of Competing Interest

The authors declare that they have no known competing financial interests or personal relationships that could have appeared to influence the work reported in this paper.

References

[1] Islam M, Islam MT, Samsuzzaman M, Faruque MRI. Compact metamaterial antenna for UWB applications. Electron Lett 2015;51:1222–4.
[2] il Kwak S, Sim D-U, Kwon JH, Yoon YJ. Design of PIFA with metamaterials for body-SAR reduction in wearable applications. IEEE Trans Electromagn Compat 2016;59:297–300.
[3] Chen M, Jiang H, Zhang H, Li D, Wang Y. Design of an acoustic superlens using single-phase metamaterials with a star-shaped lattice structure. Sci Rep 2018;8:1861.
[4] Zheng Z, Wang W, Zhang H-T, Zheng Y-Y, Liang X-L. Dual-band anti-interference slot antenna using metamaterial structure. 2019 IEEE International Symposium on Antennas and Propagation and USNC-URSI Radio Science Meeting. 2019. p. 327–8.
[5] Zhao G, Bi S, Niu M, Cui Y. A zero refraction metamaterial and its application in electromagnetic stealth cloak. Mater Today Commun 2019;21:100603.
[6] Baqir M, Choudhury PK. Hyperbolic metamaterial-based UV absorber. IEEE Photonics Technol Lett 2017;29:1548–51.
[7] Liu W, Sun H, Xu L. A microwave method for dielectric characterization measurement of small liquids using a metamaterial-based sensor. Sensors 2018;18:1438.
[8] Pendry JB, Holden AJ, Robbins DJ, Stewart W. Magnetism from conductors and enhanced nonlinear phenomena. IEEE Trans Microw Theory Tech 1999;47:2075–84.
[9] Sabah C, Nesimoglu T. Design and characterization of a resonator-based metamaterial and its sensor application using microstrip technology. Opt Eng 2016;55:027107.
[10] Hossain MJ, Faruque MRI, Islam MT. Design and analysis of a new composite double negative metamaterial for multi-band communication. Curr Appl Phys 2017;17:931–9.
[11] Zarghooni B, Dadgarpour A, Denidni TA. Greek-key pattern as a miniaturized multiband metamaterial unit-cell. IEEE Antennas Wirel Propag Lett 2015;14:1254–7.
[12] Marathe D, Kulat K. A compact triple-band negative permittivity metamaterial for C, X-band applications. Int J Antennas Propagation 2017;2017.
[13] Smith KL, Adams RS. Spherical spiral metamaterial unit cell for negative permeability and negative permittivity. IEEE Trans Antennas Propag 2018;66:6425–8.
[14] Misran N, Yusop SH, Islam MT, Ismail MY. Analysis of parameterization substrate thickness and permittivity for concentric split ring square reflectarray element. Jurnal Kejuruteraan (J Eng) 2012;23:11–6.
[15] Rezaeieh SA, Antoniades MA, Abbosh AM. Bandwidth and directivity enhancement of loop antenna by nonperiodic distribution of mu-negative metamaterial unit cells. IEEE Trans Antennas Propag 2016;64:3319–29.
[16] Amiri R, Zarghooni B, Dadgarpour A, Pourahmadazar J, Denidni TA. Anisotropic metamaterial unit-cell for millimeter-wave applications. 2016 17th International Symposium on Antenna Technology and Applied Electromagnetics (ANTEM). 2016. p. 1–2.
[17] Hossain TM, Jamlos MF, Jamlos MA, Soh PJ, Islam MI, Khan R. Modified H-shaped DNG metamaterial for multiband microwave application. Appl Phys A 2018;124:183.
[18] Islam MS, Samsuzzaman M, Beng GK, Misran N, Amin N, Islam MT. A gap coupled hexagonal split ring resonator based metamaterial for S-band and X-band microwave applications. IEEE Access 2020;8:68239–53.
[19] Almutairi AF, Islam MS, Samsuzzaman M, Islam MT, Misran N, Islam MT. A complementary split ring resonator based metamaterial with effective medium ratio for C-band microwave applications. Results Phys 2019;15:102675.
[20] Azeez AR, Elwi TA, AL-Hussain ZAA. Design and analysis of a novel concentric rings based crossed lines single negative metamaterial structure. Eng Sci Technol, Int J 2017;20:1140–6.
[21] Tamim AM, Faruque MRI, Alam MJ, Islam SS, Islam MT. Split ring resonator loaded horizontally inverse double L-shaped metamaterial for C-, X-and Ku-Band Microwave applications. Results Phys 2019;12:2112–22.
[22] Ramachandran T, Faruque MRI, Ahamed E, Abdullah S. Specific absorption rate reduction of multi split square ring metamaterial for L-and S-band application. Results Phys 2019;15:102668.
[23] Yao G, Ling F, Yue J, Luo C, Ji J, Yao J. Dual-band tunable perfect metamaterial absorber in the THz range. Opt Express 2016;24:1518–27.
[24] Ahamed E, Faruque MRI, Mansor MFB, Islam MT. Polarization-dependent tunneled metamaterial structure with enhanced fields properties for X-band application. Results Phys 2019;15:102530.
[25] Yi Z, Chen J, Cen C, Chen X, Zhou Z, Tang Y, et al. Tunable graphene-based plasmonic perfect metamaterial absorber in the THz region. Micromachines 2019;10:194.
[26] Rezapour M, Rashed-Mohassel JA, Keshtkar A, Moghadasi M-N. Suppression of mutual coupling in rectangular dielectric resonator antenna arrays using Epsilon-Negative metamaterials (ENG). J Electromagnetic Waves Appl 2019;33:1211–23.
[27] Islam MR, Samsuzzaman M, Misran N, Beng GK, Islam MT. A tri-band left-handed meta-atom enabled designed with high effective medium ratio for microwave based applications. Results Phys 2020:103032.
[28] Liu P, Yang S, Jain A, Wang Q, Jiang H, Song J, et al. Tunable meta-atom using liquid metal embedded in stretchable polymer. J Appl Phys 2015;118:014504.
[29] Zhou Z, Yang H. Triple-band asymmetric transmission of linear polarization with deformed S-shape bilayer chiral metamaterial. Appl Phys A 2015;119:115–9.
[30] Alam MJ, Ahamed E, Faruque MRI, Islam MT, Tamim AM. Left-handed metamaterial bandpass filter for GPS, Earth Exploration-Satellite and WiMAX frequency sensing applications. PloS one 2019;14.
[31] Hoque A, Tariqul Islam M, Almutairi AF, Alam T, Jit Singh M, Amin N. A polarization independent quasi-TEM metamaterial absorber for X and ku band sensing applications. Sensors 2018;18:4209.
[32] Bait-Suwailam MM. Electromagnetic Field Interaction with Metamaterials. Electromagnetic Fields and Waves. IntechOpen; 2019.
[33] Chen X, Grzegorczyk TM, Wu B-I, Pacheco Jr J, Kong JA. Robust method to retrieve the constitutive effective parameters of metamaterials. Phys Rev E 2004;70:016608.
[34] Nicolson A, Ross G. Measurement of the intrinsic properties of materials by time-domain techniques. IEEE Trans Instrum Meas 1970;19:377–82.
[35] Weir WB. Automatic measurement of complex dielectric constant and permeability at microwave frequencies. Proc IEEE 1974;62:33–6.
[36] Ziolkowski RW. Design, fabrication, and testing of double negative metamaterials. IEEE Trans Antennas Propag 2003;51:1516–29.
[37] Wartak MS, Tsakmakidis KL, Hess O. Introduction to metamaterials. Phys Canada 2011;67:30–4.
[38] Hasan MM, Faruque MRI, Islam MT. Beam steering of eye shape metamaterial design on dispersive media by FDTD method. Int J Numer Modell 2018;31:e2319.
[39] Gay-Balmaz P, Martin OJ. Electromagnetic resonances in individual and coupled split-ring resonators. J Appl Phys 2002;92:2929–36.
[40] Kim IK, Varadan VV. Electric and magnetic resonances in symmetric pairs of split ring resonators. J Appl Phys 2009;106:074504.
[41] Pendry JB, Holden A, Stewart W, Youngs I. Extremely low frequency plasmons in metallic mesostructures. Phys Rev Lett 1996;76:4773.
[42] Dawar P, De A. Bandwidth enhancement of RMPA using ENG metamaterials at THz. 2013 4th International Conference on Computer and Communication Technology (ICCCT). 2013. p. 11–6.
[43] Abdel-Rahman AB, Ibrahim AA, Metamaterial enhances microstrip antenna gain,

2016.
[44] Bouzouad M, Chaker S, Bensafielddine D, Laamari E. Gain enhancement with near-zero-index metamaterial superstrate. Appl Phys A 2015;121:1075–80.
[45] Enoch S, Tayeb G, Sabouroux P, Guérin N, Vincent P. A metamaterial for directive emission. Phys Rev Lett 2002;89:213902.
[46] Abirami N, Joseph Wilson K. Analysis of properties of metamaterial-based composite system. Int J Mod Phys B 2019;33:1950154.
[47] Ramachandran T, Faruque MRI, Islam MT. A dual band left-handed metamaterial-enabled design for satellite applications. Results Phys 2020;16:102942.
[48] Hasan M, Faruque MRI, Islam SS, Islam MT. A new compact double-negative miniaturized metamaterial for wideband operation. Materials 2016;9:830.